


## RESEARCH ARTICLE

 View Article Online  
View Journal | View Issue

 Cite this: *Mater. Chem. Front.*,  
2022, 6, 1824

# Triple optically modulated and enzymatically responsive organic afterglow materials for dynamic anti-counterfeiting†

 Haijiang Qiu,<sup>ab</sup> Wensong Wang,<sup>ab</sup> Hongrui Cheng,<sup>ab</sup> Yongfeng Lu,<sup>ab</sup> Min Li,<sup>ab</sup>  
Haixin Chen,<sup>ab</sup> Xiao Fang,<sup>ab</sup> Cheng Jiang <sup>\*cd</sup> and Yuanhui Zheng <sup>\*ab</sup>

Luminescent anti-counterfeiting is one of the extensively used strategies to combat the growing serious global forgery issue in modern society. Although many luminescent security labels have been developed, the majority of them are static and can be readily cloned due to their deterministic decoding mechanism. Therefore, an advanced dynamic anti-counterfeiting strategy is urgently needed. Herein, a multiple optical and biological response based label is developed for the first-time using *o*-phenylenediamine doped cyanuric acid as the information carrier that shows artificial enzyme activity and triple optical responses, *i.e.*, fluorescence, thermally activated delayed fluorescence (TADF) and phosphorescence. The optical properties of the security label can be reversibly modulated with excitation-wavelength, temperature and time, respectively, and irreversibly modulated by enzymatic discoloration, making it difficult to duplicate. The fabricated organic information carrier shows multiple optical properties compared to the traditional TADF or phosphorescent materials with limited information encryption, making it more favorable for anti-counterfeiting. The visually verifiable afterglow label bearing multiple dynamic encrypted messages offers bright prospects for high-security-level anti-counterfeiting applications.

 Received 15th March 2022,  
Accepted 20th May 2022

DOI: 10.1039/d2qm00235c

rsc.li/frontiers-materials

## Introduction

In recent years, anti-counterfeiting techniques have attracted tremendous attention from governments, business organizations, and customers due to the increasing number of fake and shoddy products.<sup>1–5</sup> The counterfeiting business is widespread in the manufacturing of products ranging from counterfeit currency to daily necessities, to pharmaceuticals, luxuries, and high-tech devices. The related products from illegal channels have caused great economic losses. For example, as claimed by the Global Brand Counterfeiting Report 2018, the total global economic losses from counterfeiting reached \$1.2 trillion in 2017 and rocketed to \$1.82 trillion in 2020.<sup>1</sup> In response to the severe situation, many security labels, such as

topographical markers,<sup>6</sup> luminescent labels,<sup>7–10</sup> luminescent magnetic labels,<sup>11–13</sup> and plasmonic security taggants,<sup>4,14,15</sup> have been developed to protect valuable documents and brands. Among these, luminescence anti-counterfeiting is one of the commercialized techniques with benefits of relatively high photostability, multicolor, facile design, and easy to visualize by eye or read using an authentication tool such as a digital camera or a spectrometer.<sup>16</sup> A luminescent security label is usually produced by printing specific optical materials, such as carbon quantum dots,<sup>17–19</sup> metal-organic frameworks,<sup>20–22</sup> coordination polymers,<sup>23–25</sup> organic dyes,<sup>26,27</sup> and up-conversion nanoparticles,<sup>28–30</sup> as information carriers. Unfortunately, fluorescent security labels usually fall into the class of static and single-encrypted messages, which are at high-risk of being replicated, thus offering compromised protection for the products.<sup>31</sup>

To address this issue, afterglow materials have been proposed and introduced in optical encryption as a promising alternative. These afterglow material-based labels possess merits of dynamic patterns and tunable color under irradiation, making them difficult to duplicate by counterfeiters.<sup>32,33</sup> Although a large number of afterglow materials have been fabricated, metal-free afterglow materials are particularly interesting in the field of anti-counterfeiting owing to the

<sup>a</sup> College of Chemistry, Fujian Provincial Key Laboratory of Advanced Inorganic Oxygenated Materials, Fuzhou University, Fuzhou 350116, China.  
E-mail: Yuanhui.Zheng@fzu.edu.cn

<sup>b</sup> Fujian Science & Technology Innovation Laboratory for Optoelectronic Information, 350116, China

<sup>c</sup> School of Life and Health Sciences, The Chinese University of Hong Kong, Shenzhen, 518172, China. E-mail: cheng.jiang@ndcn.ox.ac.uk

<sup>d</sup> Department of Chemistry, University of Oxford, Oxford, OX1 3QZ, UK

† Electronic supplementary information (ESI) available. See DOI: <https://doi.org/10.1039/d2qm00235c>

advantages of abundance and low price of raw materials, low-toxicity and easy-modulation of luminescence properties. For instance, carbonyl functional group room temperature phosphorescence (RTP) materials have made remarkable achievements in advanced dynamic information encryption.<sup>34,35</sup> However, phosphorescent carbonyl compounds still suffer from obvious limitations, *e.g.*, short lifetime, photobleaching, and poor water stability.<sup>36</sup> Compared to the phosphorescent carbonyl compounds, pure organic afterglow materials with longer lifetime, higher stability and resource of eco-friendly material makes it possible to encode optical information on space or time scales.<sup>37–39</sup> More encouragingly, a color-tunable dual-mode afterglow label proposed by the Zhao group and the Xu group further improves the anti-counterfeiting performance of traditional labels.<sup>40,41</sup> Ren and Qu designed a time-dependent phosphorescent color material to create a 3D code for dynamic information encryption.<sup>42</sup> Huang *et al.* have reported a colorful phosphorescent material to create a 4D code for information encryption.<sup>43</sup> These examples show that the more information a material can carry, the higher will be its encoding capacity and level of security. Although significant progress in optical encryption based on dual-/multi-mode responses of the composite afterglow materials under various external stimuli (such as excitation light,<sup>44–47</sup> heat,<sup>48</sup> mechanical force,<sup>49</sup> chemical reagents,<sup>50</sup> *etc.*) has been made, achieving all these properties in a single material remains a major challenge. Inspired by the recent study using dopant-matrix collaboration, molecular doping may lead to the enhancement of phosphorescence of an organic material and prolongation of its phosphorescence lifetime.<sup>51</sup> Cyanuric acid (CA) may be a great candidate as a host material for molecular doping to achieve water-resist afterglow materials with long lifetime because it forms crystals that have weak RTP and are chemically stable in water *via* intermolecular hydrogen bonds.<sup>52,53</sup> Based on the above considerations, we speculated that if we introduce a suitable molecule into the skeleton of CA through hydrogen bonding, its phosphorescence emission and lifetime could be greatly enhanced in both air and aqueous environments. *o*-Phenylenediamine (oPD) is considered as a good doping molecule that carries two amino groups and a benzene ring, which can easily form hydrogen bonds and provide impurity energy levels, respectively. As a verification experiment, a novel oPD doped CA organic afterglow material with triple optical response and enzymatically responsive was synthesized.

## Experimental

### Materials and chemicals

All chemicals and solvents were commercially purchased and used as received without further purification. Potassium chloride (KCl), *o*-phenylenediamine (C<sub>6</sub>H<sub>8</sub>N<sub>2</sub>), cyanuric acid (C<sub>3</sub>H<sub>3</sub>N<sub>3</sub>O<sub>3</sub>), lithium chloride (LiCl) and methyl sulfoxide-d<sub>6</sub> (C<sub>2</sub>D<sub>6</sub>OS) were purchased from Energy Chemical (China). Melamine (C<sub>3</sub>H<sub>6</sub>N<sub>6</sub>), formic acid (CH<sub>2</sub>O<sub>2</sub>) and polyvinyl acetate (PVCA) were purchased from Sinopharm Chemical Reagent

Co., Ltd (China). 3,3',5,5'-Tetratmethylbenzidine (C<sub>16</sub>H<sub>22</sub>Cl<sub>2</sub>N<sub>2</sub>) was purchased from Mackmin (China).

### Preparation of oPD Doped g-C<sub>3</sub>N<sub>4</sub> supramolecule

Melamine (2.523 g, 20 mmol) and *o*-phenylenediamine (0.06 g, 0.5 mmol) were fully ground with potassium chloride (2.7 g, 63.7 mmol) and lithium chloride (3.3 g, 63.7 mmol) in a mortar. The mixed precursors were transferred into a porcelain boat and heated to 350 °C using a muffle furnace with a heating rate of 5 °C min<sup>-1</sup> and kept at this temperature for 4 hours. The whole process was protected by a N<sub>2</sub> atmosphere (flow rate 50 mL min<sup>-1</sup>). Finally, yellow powders were obtained, named PCN.

### Preparation of oPD-CA

0.5 g of PCN was dissolved in 10 mL formic acid with the aid of ultrasonication for 10 minutes. Then, the homogeneous solution was transferred to a 25 mL of stainless-steel teflon-lined autoclave and heated to 180 °C for 24 hours. The product was cooled down to room temperature and washed with ultra-pure water three times. Finally, the product was dried in an oven at 60 °C for 12 hours and pale-yellow crystals were obtained, named oPD-CA.

### Preparation of the solution of TMB-H<sub>2</sub>O<sub>2</sub>

Take 40 μL of H<sub>2</sub>O<sub>2</sub> droplets into 40 mL of water and shake them to obtain a mixed solution. Then add 20 mg of TMB to the mixed solution, stir until it is completely dissolved, and get 0.5 g L<sup>-1</sup> of TMB solution.

### Preparation of the dynamic anticounterfeiting labels

PVCA was used as the matrix for the oPD-CA material. First, 0.5 g oPD-CA powders were dispersed in 0.5 g PVCA and mechanical stirring was performed for 10 min. Then, the mixture was printed on a A4 paper by film printing. Finally, after curing at room temperature for 10 min, PVCA-based multiple-dimension luminescence images for dynamic anti-counterfeiting labels were obtained.

### Characterizations

Powder X-ray diffraction (XRD) patterns of the as-prepared samples were recorded with a Bruker D8 advance X-ray diffractometer using Cu K $\alpha$  radiation. FTIR spectra were recorded in the range 400–4000 cm<sup>-1</sup> on a Nicolet iS50 FT-IR spectrophotometer. Thermogravimetric-differential scanning calorimetric analysis (TG-DSC) was done using a TGA/DSC<sup>3+</sup> system (METTLER TOLEDO) in the nitrogen atmosphere to investigate the thermal stability and difference of the samples. X-ray photoelectron spectroscopy (XPS) measurements were performed on a VG ESCALAB 250 spectrometer with a monochromatic Al K $\alpha$  X-ray source. Nuclear magnetic resonance spectroscopy was performed on a 500 MHz spectrometer (JNM-ECZ500R/S1). The morphology and microstructure were studied using a high-resolution transmission electron microscope (FEI Talos F200S G2). The absorption of the samples was measured by a UV-visible diffuse reflectance spectrometer (Cary 500, Varian Co.) using BaSO<sub>4</sub> as the reference. Steady-state

fluorescence/phosphorescence spectra, excitation spectra lifetimes and time-resolved emission spectra were obtained using a fluorophotometer (Edinburgh FL/FS980) equipped with a xenon arc lamp (Xe 900) and a microsecond flash-lamp ( $\mu$ F900), respectively. The photoluminescence quantum efficiency was recorded by a Hamamatsu Absolute PL Quantum Yield Spectrometer C11347. The phosphorescence quantum yield was obtained by eqn (1),

$$\varphi_{\text{Phos.}} = \frac{B}{A} \times \varphi_{\text{PL}} \quad (1)$$

In eqn (1),  $\varphi_{\text{phos.}}$  and  $\varphi_{\text{PL}}$  represent the phosphorescence quantum yield and absolute photoluminescence quantum yield, respectively.  $A$  and  $B$  are the integral area of total photoluminescence and phosphorescence spectra, respectively. The photos of fluorescence and phosphorescence emission were recorded by a digital camera SONY DSC-HX400.

## Results and discussion

### Synthesis and characterization of small molecules doped CA

It has been previously reported that graphite-phase carbon nitride ( $g\text{-C}_3\text{N}_4$ ) can be transformed to colorless CA crystals through hydrothermal synthesis.<sup>54</sup> Therefore, it is believed that

small organic molecule doped CA crystals could also be synthesized in the same way. To probe this notion, *o*-phenylenediamine (oPD) doped graphitic carbon nitride (named PCN) was fabricated by molten salt treatment (350 °C, 4 h) of melamine and oPD, the resultant mixture was then subjected to a hydrothermal treatment (180 °C, 24 h) (see Scheme S1 for the synthesis process), yielding faint yellow columnar crystals (named oPD-CA) (see Fig. S1a and b, ESI<sup>†</sup>). Sub-micron particles with bulk morphology were observed from the TEM image (see Fig. S1c and d, ESI<sup>†</sup>). It should be noted that these particles can be easily damaged upon electron beam irradiation during the TEM measurement (see Fig. S1d, ESI<sup>†</sup>), which indicates that they are organic materials.<sup>55,56</sup> The oPD-CA crystals were ground into powder to examine the powder X-ray diffraction (XRD) pattern, <sup>13</sup>C-NMR and Fourier transform infrared (FTIR) spectra in comparison to those of CA and oPD samples (Fig. 1a–c). (1) Strong diffraction peaks were observed at about 19.8°, 22.44°, 26.4°, and 29.8°, which correspond to (111), (002), (020) and (202) crystal facets of the CA matrix, respectively. They all shift to smaller diffraction angles ( $\sim 0.3^\circ$ ) compared to those of the pristine CA crystals. (2) In the <sup>13</sup>C-NMR spectra, oPD-CA shows a major chemical shift for CA located at 135 ppm and three weak chemical shifts for oPD located at 135, 117 and 115 ppm, which confirms the doping of oPD into CA.

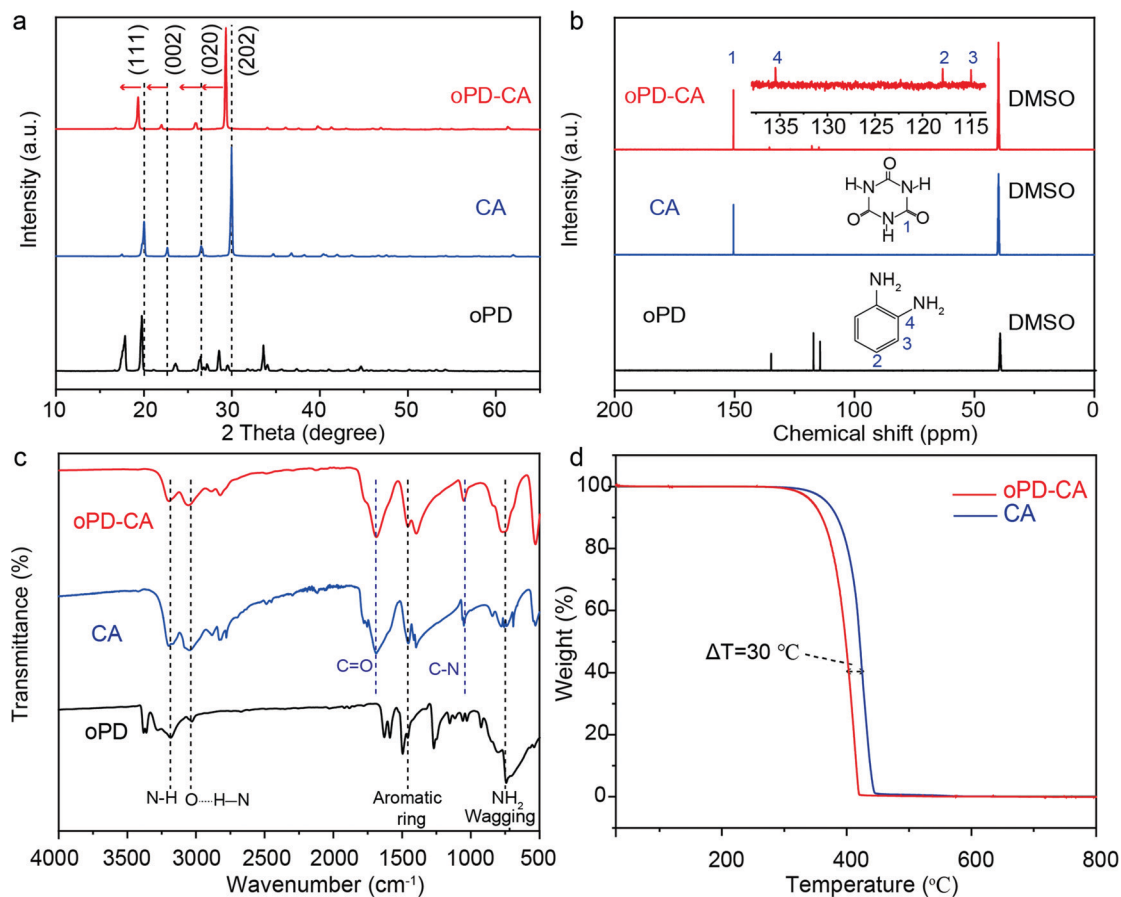


Fig. 1 (a) Powder XRD patterns, (b) <sup>13</sup>C-NMR spectra, (c) FTIR spectra of as-synthesized oPD-CA, pristine CA, and oPD, and (d) TG curves of oPD-CA, and the pristine CA in the nitrogen environment.

According to the external standard method (see Fig. S2, ESI† for calculation details), the experimental molecular doping concentration is calculated to be 96:1 (molar ratio of CA: oPD), which is lower than the theoretical value of 40:1. (3) All the diffraction peaks and FTIR absorption peaks of oPD-CA are well matched with those of the pristine CA crystals, but a distinct amino ( $-\text{NH}_2$ ) wagging band ( $741\text{ cm}^{-1}$ ) and an aromatic ring ( $1262\text{ cm}^{-1}$  and  $1500\text{ cm}^{-1}$ ) were observed. Moreover, the peak intensity of the hydrogen bond at  $3046\text{ cm}^{-1}$  is significantly increased (see Note S1 and Fig. S3, ESI† for calculation details). Thermogravimetry (TG) measurements were carried out to determine the weight percentage of the oPD dopant. Fig. 1d compares the TG curves of oPD-CA and CA. Obviously, both of oPD-CA and CA are thermally stable below  $300\text{ }^\circ\text{C}$  in air. The main difference between the two samples is that the complete-decomposition temperature of oPD-CA decreases by  $\sim 30\text{ }^\circ\text{C}$  compared to CA. This indicated that oPD was successfully doped into the CA matrix and it reduced the thermal stability of oPD-CA. Other molecules (*e.g.*, catechol) can also be doped in CA, forming an organic afterglow material with different optical properties (see Fig. S4, ESI†).

X-Ray photoelectron spectroscopy (XPS) analysis was carried out to gain insight into the chemical structure of oPD-CA and

CA samples (Fig. 2). In the survey spectra, C, N, and O elements are observed for both of oPD-CA and CA (Fig. 2a). The peak fitting of the high-resolution  $\text{C}_{1s}$  peaks reveals that there are three carbon species with binding energies at  $284.8\text{ eV}$ ,  $286.3\text{ eV}$ , and  $289.9\text{ eV}$ , which are assigned to  $\text{C}=\text{C}/\text{C}-\text{C}$  carbon bonds,  $\text{C}-\text{N}$  species and  $\text{sp}^2$ -bond carbon ( $\text{C}=\text{O}$ ), respectively (Fig. 2b).<sup>54</sup> Fig. 2c shows the high-resolution  $\text{N}_{1s}$  XPS spectra of oPD-CA and CA, in which two types of nitrogen species with binding energy at  $400.7\text{ eV}$  and  $402.0\text{ eV}$  are observed for the two samples. However, a new peak of  $\text{Ph}-\text{NH}_2$  with binding energy at  $399.2\text{ eV}$  is only detected for oPD-CA. In addition, the  $\text{O}_{1s}$  can be deconvoluted into two peaks, responding to  $\text{C}=\text{O}$  species at  $532.2\text{ eV}$  and  $\text{C}-\text{O}$  at  $533.3\text{ eV}$ , respectively (Fig. 2d). The higher  $\text{C}_{1s}$  intensity of  $\text{C}=\text{C}$  ( $\text{sp}^2$ ) carbon bonds and the presence of  $\text{Ph}-\text{NH}_2$  species for oPD-CA reveal the successful doping of oPD into the CA matrix, which is in good agreement with the XRD,  $^{13}\text{C}$ -NMR spectra, FTIR and TG data.

### Optical properties of oPD-CA

The synthesized oPD-CA crystals exhibit three different optical responses, *i.e.*, fluorescence, TADF and phosphorescence (Fig. 3a-f). The wavelength-dependent luminescence spectra of oPD-CA at room temperature were recorded wherein the

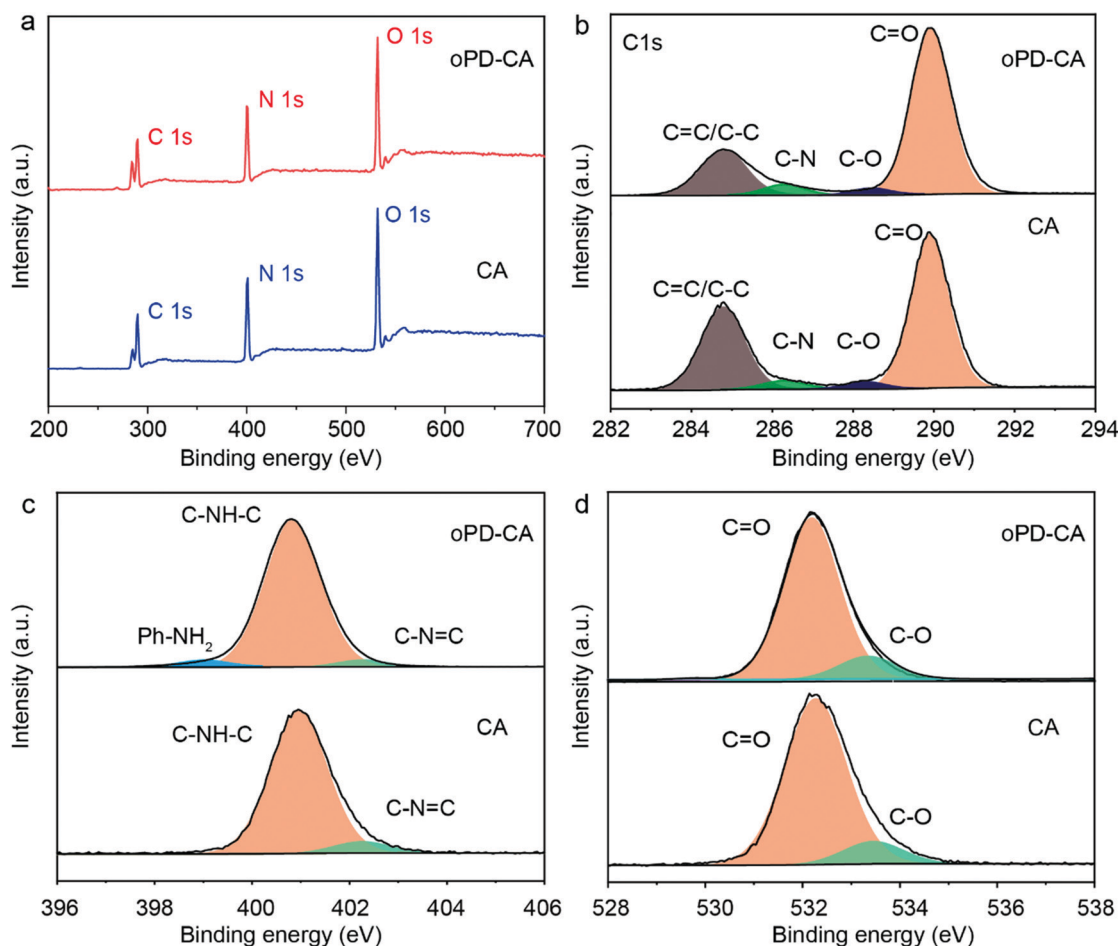
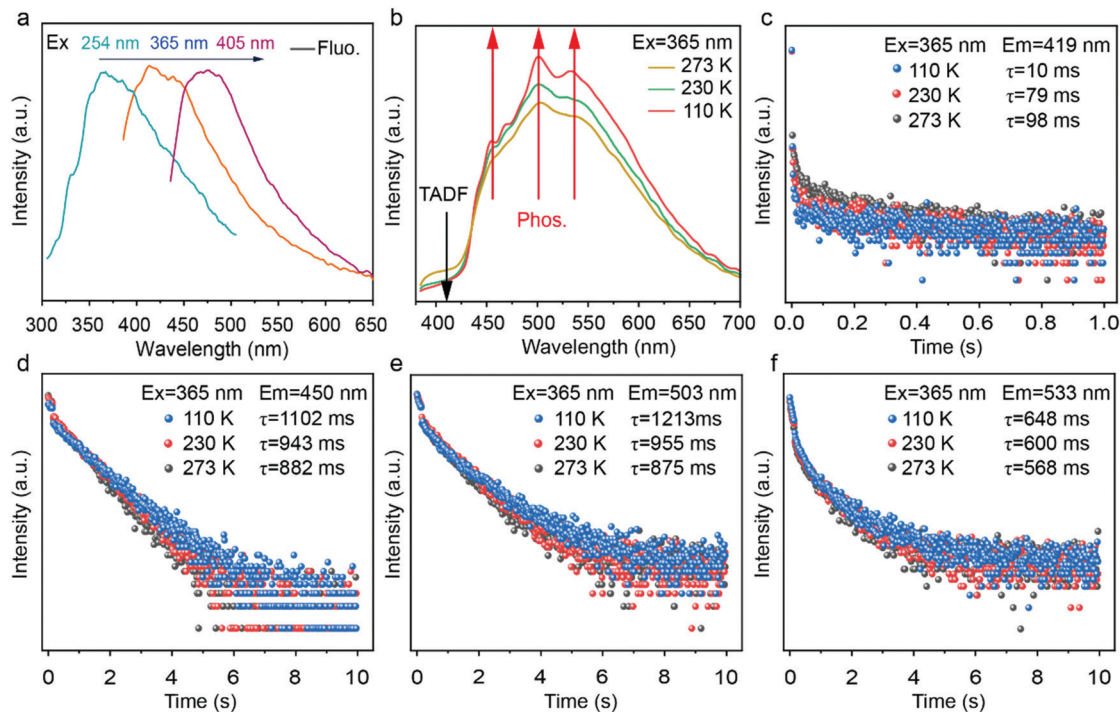


Fig. 2 XPS spectra of oPD-CA and CA for (a) survey scan, (b)  $\text{C}_{1s}$ , (c)  $\text{N}_{1s}$ , and (d)  $\text{O}_{1s}$ .



**Fig. 3** (a) Excitation wavelength dependent room-temperature fluorescence spectra, (b) temperature-dependent afterglow spectra, (c) TADF decay kinetics, (d) phosphorescence decay kinetics for 450 nm, (e) phosphorescence decay kinetics for 503 nm, and (f) phosphorescence decay kinetics for 533 nm.

red-shift of an emission peak happens upon an increase in excitation wavelength (Fig. 3a). Interestingly, a strong green and cyan afterglow of the oPD-CA powder in air or in water was observed by naked eyes after the removal of an ultraviolet (UV) lamp for 0.1 s and 1 s, respectively (see Fig. S5, ESI<sup>†</sup>). In contrast, only a very weak blue afterglow of the pristine CA powder was observed only in air but not in water (see Fig. S6, ESI<sup>†</sup>). Obviously, the doping of oPD has significantly enhanced the afterglow of the CA matrix. Under 365 nm light excitation, the fluorescence quantum yield and phosphorescence quantum yield of oPD-CA were recorded as 10.5% and 14.2%, respectively (see Table S1, ESI<sup>†</sup>). To understand the temperature-dependent afterglow behavior of oPD-CA, its afterglow spectra were obtained under UV (365 nm) excitation at different temperatures (Fig. 3b). Four emission peaks at 419 nm, 450 nm, 503 nm and 533 nm were observed. The position of the shoulder peak (Fig. 3b, black curve) is almost identical to that of its fluorescence emission peak under the same excitation conditions. Surprisingly, the emission intensities of the three peaks shown in Fig. 3b evolve in an opposite trend with the decrease of temperature. More specifically, the emission intensity of the shoulder peak drops, while that of the main peak increases, indicating that the origin of the first peak is different from the other three peaks. It is believed that the shoulder peak is assigned to TADF, while the other peak is attributed to the phosphorescence.<sup>57,58</sup> Fig. 3c–f show the emission decay profiles of TADF and phosphorescence components of oPD-CA at different temperatures. All the

afterglow-lifetime decay curves can be well fitted by tri-exponential decay (see Tables S2 and S3, ESI<sup>†</sup>). The average lifetimes were calculated by the following eqn (2):

$$\tau = \frac{\sum a_i \tau_i^2}{\sum a_i \tau_i} \quad (2)$$

where  $\tau_i$  represents a luminescent component with different lifetimes (*i.e.*,  $\tau_1$ ,  $\tau_2$  and  $\tau_3$ ).  $a_i$  is the initial strength of each component (amplitudes) of the lifetime ( $\tau_i$ ).<sup>59</sup>

The calculated lifetimes are 10 ms, 79 ms, and 98 ms for TADF, 1102 ms, 943 ms and 882 ms for the phosphorescence of 450 nm, 1213 ms, 955 ms and 875 ms for the phosphorescence of 503 nm and 648 ms, 600 ms and 568 ms for the phosphorescence of 533 nm at 273 K, 230 K, and 110 K, respectively, under excitation at 365 nm and the slit size for the excitation and emission wavelength 7 nm and 7 nm, respectively. Due to the shorter lifetime at emission wavelengths 419 nm and 533 nm, the yellow-green composite afterglow can be observed first. Conversely, the cyan complex afterglow can be observed later due to longer lifetimes at emission wavelengths of 450 nm and 503 nm. It explains well the reason why oPD-CA has a yellow-green and a cyan afterglow, after 365 nm light irradiation. These unique triple-mode emission phenomena (*i.e.*, fluorescence, TADF and phosphorescence) of the novel organic oPD-CA material pave a good way for advanced anti-counterfeiting applications due to the encoding of multi-dimensional dynamical optical information.

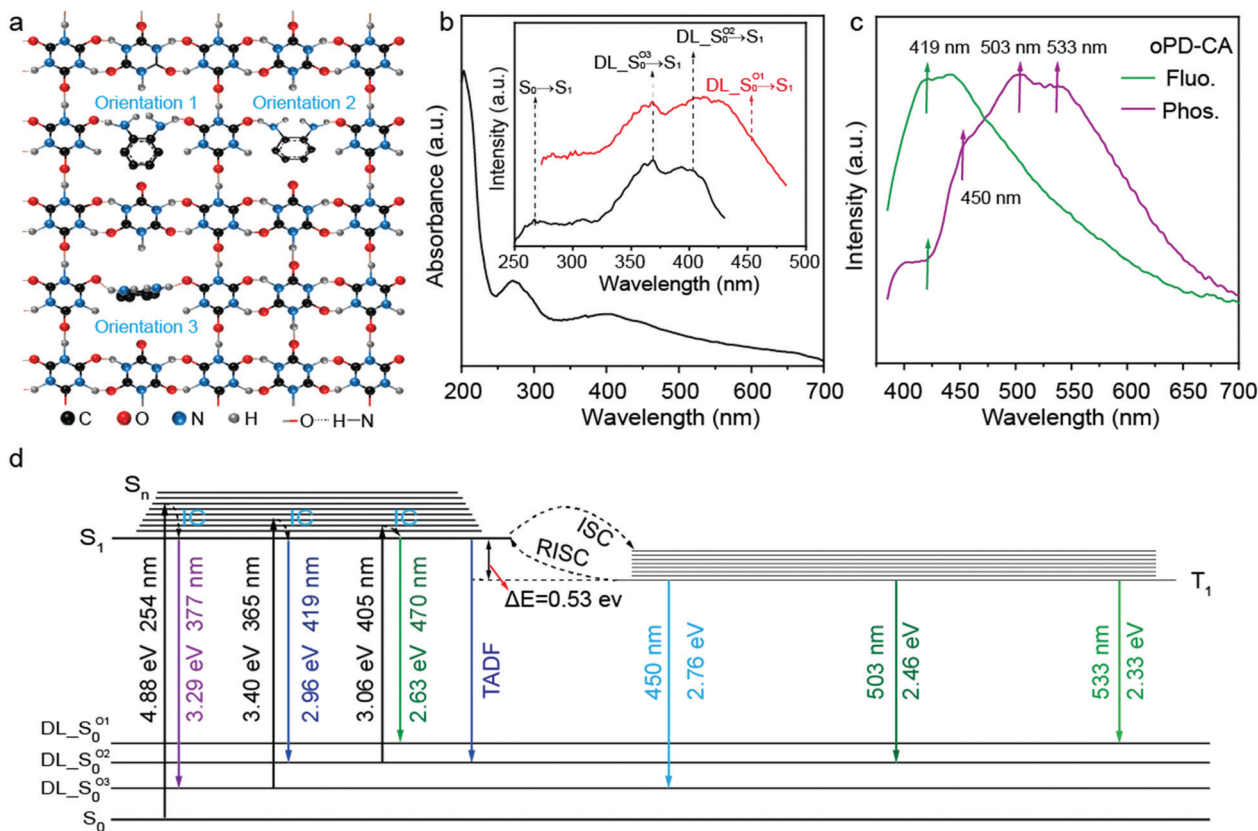


Fig. 4 The role of the oPD dopant for the triple-mode emissions: (a) The proposed chemical structure, (b) diffuse reflectance spectrum of oPD-CA, and the inset represents the excitation spectrum of oPD-CA at 450 nm and 503 nm emission wavelength, (c) afterglow spectra of oPD-CA at room temperature, and (d) luminescence mechanism of oPD-CA.

### Luminescence mechanism of oPD-CA

Fig. 4a illustrates the proposed molecular structure of oPD-CA crystals. As shown in Fig. 4a, the oPD molecules are randomly doped in the CA matrix with different orientations by replacing some CA molecules in the lattice. To understand the role of the dopant oPD for the observed triple-mode emissions, we studied the diffuse reflectance spectroscopy (DRS), excitation, fluorescence and phosphorescence properties of oPD-CA at the room temperature (Fig. 4b and c). As shown in Fig. 4b, there are two broad absorption peaks at around 270 nm and 400 nm. Four excitation peaks correspond to the transitions from the new ground states (*i.e.*,  $S_0$  and the three doping levels) to  $S_1$  of CA. (see the inset of Fig. 4b). Under the excitation of 365 nm light, the maximum fluorescence emission peak of oPD-CA is located at 419 nm, and the phosphorescence peaks are located at 450 nm, 503 nm and 533 nm, respectively. Moreover, a weak delayed fluorescence can be observed around 419 nm (Fig. 4c).

Since CA itself shows a weak blue afterglow in air (see Fig. S6, ESI<sup>†</sup>), both the singlet state ( $S_1$ ) and the triplet state ( $T_1$ ) must co-exist in the system. The doping of oPD into the system inevitably introduces new doping levels, which may originate from the orientation of the dopant molecule.<sup>60</sup> According to Kasha's rule,<sup>61</sup> photon emission should occur only from the lowest excited states of the luminescent material ( $S_1$  and/or triplet state  $T_1$ ) to its ground states ( $S_0$ ). The observance of the

red-shift of the fluorescent ( $S_1$ - $S_0$  transitions) and phosphorescent ( $T_1$ - $S_0$  transitions) emissions for the doped CA indicates that the doped energy levels should locate close to the original  $S_0$  level of CA, forming new ground states. Based on the luminescence properties of oPD-CA shown in Fig. 3a and b as well as the absorption and excitation spectra shown in Fig. 4b, we proposed a possible luminescence mechanism of oPD-CA to explain the observed triple optical responses. As shown in Fig. 4d, under UV light irradiation, the excited electrons are relaxed to the  $S_1$  state through the direct internal conversion (IC) process, and partial electrons return to the new ground states (*i.e.*,  $S_1 \rightarrow DL_{S_0}^{01}$ ,  $S_1 \rightarrow DL_{S_0}^{02}$  and  $S_1 \rightarrow DL_{S_0}^{03}$ ) via emitting fluorescence (Fig. 3a). At the same time, some cross to the triplet excited state ( $T_1$ ) through the intersystem crossover (ISC) and return to the new ground states (*i.e.*,  $T_1 \rightarrow DL_{S_0}^{01}$ ,  $T_1 \rightarrow DL_{S_0}^{02}$  and  $T_1 \rightarrow DL_{S_0}^{03}$ ), via emitting phosphorescence (Fig. 3b and 4c). Notably, it has been reported that when the energy band difference of  $S_1$  and  $T_1$  is sufficiently small, the competition rate of the reverse intersystem crossover (RISC) at room temperature will be large enough.<sup>62,63</sup> The energy difference between  $S_1$  and  $T_1$  for the oPD-CA system is calculated to be as small as 0.53 eV. Such a small energy difference allows some electrons at  $T_1$  to go back to  $S_1$  through the RISC process by absorbing the surrounding thermal energy and eventually de-excite to the new  $DL_{S_0}^{02}$  ground state, thus emitting TADF.

Obviously, high temperature is favorable for TADF to occur, which explains the decrease of TADF intensity as the temperature drops (Fig. 3b). The unique triple-mode optical responses are dynamically tunable, making the oPD-CA material an excellent information carrier for anti-counterfeiting applications.

More encouragingly, the obtained oPD-CA also displays artificial enzyme activity besides its optical excellence. The

OPD-CA powder can make 3,3',5,5'-tetramethylbenzidine (TMB) gradually turn blue in the presence of hydrogen peroxide ( $H_2O_2$ ). Two absorption peaks at about 370 nm and 650 nm were observed and intensified with increasing reaction time, from the UV-Vis absorption spectrum (Fig. S7, ESI<sup>†</sup>). The silica powder does not change the color of the solution. The peroxidase-like catalysis was revealed by triggering the colorimetric reaction using the TMB substrate in the presence of

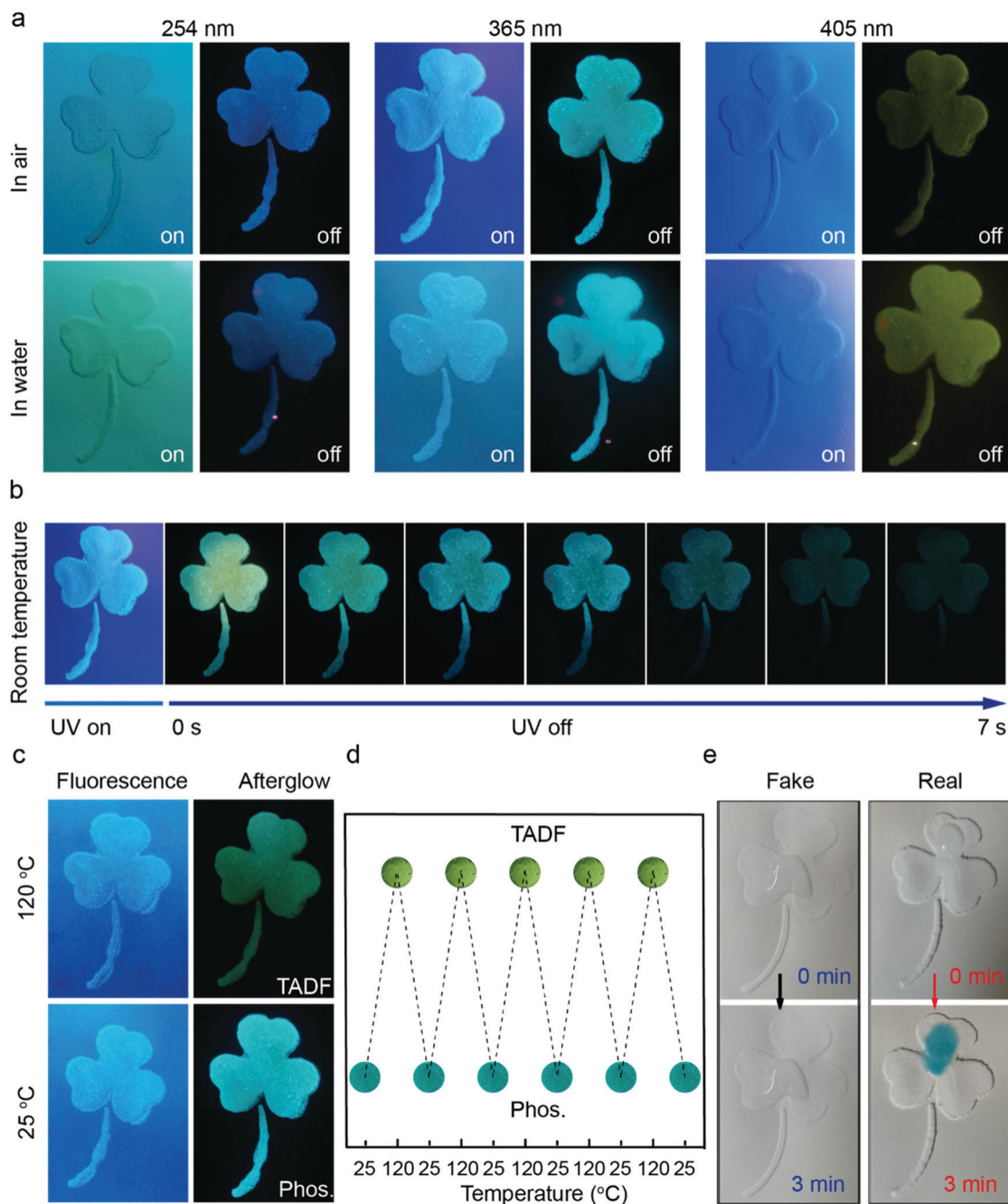


Fig. 5 Photograph of the fabricated dynamic security labels modulated with (a) excitation wavelength in air (top column) and in water (bottom column), (b) time, (c and d) temperature, and (e) TMB colorimetric detection of the fake label manufactured using  $SiO_2$  (left) and real label manufactured using oPD-CA (right).

H<sub>2</sub>O<sub>2</sub> (Fig. S8, ESI†). This is mainly attributed to the confinement of oPD inside the CA matrix-based host, which plays a vital role in the generation of catalytic activity.<sup>64–66</sup> In the present oPD-CA system, the –C=O groups could serve as the catalytic activity site and substrate-binding site, respectively.<sup>67</sup>

### Triple optically modulated and enzymatically responsive dynamic anti-counterfeiting

Intrigued by the fascinating optical properties and artificial enzyme activity of oPD-CA, we developed a quad-modulated dynamic anti-counterfeiting strategy using oPD-CA as an information carrier. The dynamic security labels with various patterns were fabricated by stencil printing of a slurry composed of polyvinyl acetate and oPD-CA on A4 paper (Fig. 5). First, the emission fluorescence and afterglow colors of the fabricated security label can be dynamically tuned with different excitation wavelengths. Fig. 5a shows the optical images of a clover pattern that is placed in air and water with UV light on and off, respectively. The pattern exhibits bright blue fluorescence at room temperature under excitation with 254 nm UV light. After turning off the UV light, the pattern area remains blue due to the phosphorescent emission, while the area surrounding the pattern turns black. When the excitation wavelength shifted to 365 nm, the color of the pattern turns cyan under both UV on and off conditions. With a further increase of excitation wavelength of 419 nm, the blue fluorescence can still be observed, while the yellow-green phosphorescence is detected by a camera. These results are consistent with the optical spectra shown in Fig. 3 wherein the emission peak red-shifts with the increase of the excitation wavelength. Such excitation wavelength modulated, and water-resistant optical properties can be used as the first layer of security (see Fig. 5a and Videos S1 and S2, ESI†). Furthermore, the excellent time-resolved encryption performance of the security label can be used as the second layer of security. As shown in Fig. 5b, the color of the clover pattern immediately changed from blue fluorescence to yellow-green phosphorescence, followed by an instant change to cyan phosphorescence within 1 s, and the phosphorescence can last for 7 s, after turning off the 365 nm UV light (see Video S3, ESI†). The intensity of the afterglow color of the security labels is able to be dynamically tuned with time, which can serve as the second layer of security. Finally, the afterglow colors of the security labels are also able to be dynamically modulated by changing the external temperatures (Fig. 5c). Although there is no obvious change in fluorescence colors under 365 nm excitation when switching the label's temperature from 25 °C to 120 °C, the afterglow color changes from cyan to blue (Fig. 5c and Video S4, ESI†). An advanced anti-counterfeiting label requires that the optical material owns not only a great color tunability but also an excellent reversibility. We, therefore, monitored the afterglow color change of the oPD-CA material by repeatedly switching the temperature between 25 °C and 120 °C using a heating plate. It is found that the afterglow color change is highly reversible (Fig. 5d) between cyan and blue. This temperature modulated afterglow colors are used as the third layer of security. The system of oPD-CA-TMB-H<sub>2</sub>O<sub>2</sub> we

present can be applied to the fourth layer of security. After adding TMB-H<sub>2</sub>O<sub>2</sub> mixed solution to the label, the true label could turn blue within three minutes (Fig. 5e, right), while the false label could not (Fig. 5e, left). Moreover, the developed anti-counterfeiting labels offer four layers of security and can be massively produced using stencil printing techniques at low cost and visual authentication. These merits make the security label difficult to counterfeit and meet the criteria and demand for advanced anti-counterfeiting.

## Conclusions

In summary, a type of unprecedented organic afterglow material, small molecule doped CA, was successfully fabricated. Our results indicate that small molecules (*e.g.*, oPD and catechol) can be doped in the lattice of CA with different orientations. Not only the phosphorescence intensity and lifetime are greatly enhanced, but also oPD-CA is endowed with the optical properties of TADF and polychromatic phosphorescence due to the formation of new ground states stemming from molecular doping. By simply changing the doping molecules, the optical properties of CA can be tailored. As proof-of-concept, we demonstrated a universal synthetic method for the fabrication of small molecule doped CA afterglow materials and a cost-effective, easily authenticated, quad-modulated (*i.e.*, artificial enzyme responsive, excitation-wavelength/temperature switchable and time-resolved) dynamic anti-counterfeiting label using oPD-CA as an information carrier. Such quadruple multi-responsive anti-counterfeiting labels are distinct from the traditional static security labels with mono-optical information encryption, making them harder to counterfeit.

## Author contributions

Q. H. J., W. S. W., C. J., and Y. H. Z. conceived the idea; Q. H. J. designed the experiments and synthesized materials; H. R. C. and Y. F. L. performed the transmission and fluorescence spectra test; M. L., X. F., and H. X. C. assisted in data analysis; Q. H. J., C. J., and Y. Z. wrote the manuscript and all authors reviewed it.

## Conflicts of interest

There are no conflicts to declare.

## Acknowledgements

We thank the Recruitment Program of Global Experts, National Natural Science Foundation of China (Grant no. 62175033 and 61775040), the Fujian Science & Technology Innovation Laboratory for Optoelectronic Information (Grant no. 2021ZZ126), the Hundred-Talent Project of Fujian, and Fuzhou University for the financial support.



## Notes and references

- 1 L. Wood, *Global Brand Counterfeiting Report*, Research and Markets, Dublin, 2018.
- 2 P. Kumar, S. Singh and B. K. Gupta, Future prospects of luminescent nanomaterial based security inks: from synthesis to anti-counterfeiting applications, *Nanoscale*, 2016, **8**, 14297–14340.
- 3 Y. Zheng, C. Jiang, S. H. Ng, Y. Lu, F. Han, U. Bach and J. J. Gooding, Unclonable Plasmonic Security Labels Achieved by Shadow-Mask-Lithography-Assisted Self-Assembly, *Adv. Mater.*, 2016, **28**, 2330–2336.
- 4 R. Arppe Tabbara, M. Tabbara and T. J. Sørensen, Versatile and validated optical authentication system based on physical unclonable functions, *ACS Appl. Mater. Interfaces*, 2019, **11**, 6475–6482.
- 5 R. Arppe Tabbara and T. J. Sørensen, Physical unclonable functions generated through chemical methods for anti-counterfeiting, *Nat. Rev. Chem.*, 2017, **1**, 1–13.
- 6 H. J. Bae, S. Bae, C. Park, S. Han, J. Kim, L. N. Kim, K. Kim, S. H. Song, W. Park and S. Kwon, Biomimetic microfingerprints for anti-counterfeiting strategies, *Adv. Mater.*, 2015, **27**, 2083–2089.
- 7 H. Cheng, X. Wei, H. Qiu, W. Wang, W. Su and Y. Zheng, Chemically stable fluorescent anti-counterfeiting labels achieved by UV-induced photolysis of nanocellulose, *RSC Adv.*, 2021, **11**, 18381–18386.
- 8 Y. Liu, F. Han, F. Li, Y. Zhao, M. Chen, Z. Xu, X. Zheng, H. Hu, J. Yao, T. Guo, W. Lin, Y. Zheng, B. You, P. Liu, Y. Li and L. Qian, Inkjet-printed unclonable quantum dot fluorescent anti-counterfeiting labels with artificial intelligence authentication, *Nat. Commun.*, 2019, **10**, 2409.
- 9 Q. Zhou, X. Qiu, X. Su, Q. Liu, Y. Wen, M. Xu and F. Li, Light-Responsive Luminescent Materials for Information Encryption Against Burst Force Attack, *Small*, 2021, **17**, e2100377.
- 10 A. O. Larin, L. N. Dvoretckaja, A. M. Mozharov, I. S. Mukhin, A. B. Cherepakhin, I. I. Shishkin, E. I. Ageev and D. A. Zuev, Luminescent Erbium-Doped Silicon Thin Films for Advanced Anti-Counterfeit Labels, *Adv. Mater.*, 2021, **33**, 2005886.
- 11 N. Katumo, L. A. Ruiz-Preciado, V. Kumar, G. Hernandez-Sosa, B. S. Richards and I. A. Howard, Anticounterfeiting Labels with Smartphone-Readable Dynamic Luminescent Patterns Based on Tailored Persistent Lifetimes in  $\text{Gd}_2\text{O}_2\text{S}:\text{Eu}^{3+}/\text{Ti}^{4+}$ , *Adv. Mater. Technol.*, 2021, **6**, 2100047.
- 12 C. Li, J. Hai, S. Li, B. Wang and Z. Yang, Luminescent magnetic nanoparticles encapsulated in MOFs for highly selective and sensitive detection of  $\text{ClO}^-/\text{SCN}^-$  and anti-counterfeiting, *Nanoscale*, 2018, **10**, 8667–8676.
- 13 B. Song, H. Wang, Y. Zhong, B. Chu, Y. Su and Y. He, Fluorescent and magnetic anti-counterfeiting realized by biocompatible multifunctional silicon nanoshuttle-based security ink, *Nanoscale*, 2018, **10**, 1617–1621.
- 14 N. Torun, I. Torun, M. Sakir, M. Kalay and M. S. Onses, Physically unclonable surfaces via dewetting of polymer thin films, *ACS Appl. Mater. Interfaces*, 2021, **13**, 11247–11259.
- 15 H. Cheng, Y. Lu, D. Zhu, L. Rosa, F. Han, M. Ma, W. Su, P. S. Francis and Y. Zheng, Plasmonic nanopapers: flexible, stable and sensitive multiplex PUF tags for unclonable anti-counterfeiting applications, *Nanoscale*, 2020, **12**, 9471–9480.
- 16 X. Yin, H. Wang, Y. Tian, M. Xing, Y. Fu and X. Luo, Three primary color emissions from single multilayered nanocrystals, *Nanoscale*, 2018, **10**, 9673–9678.
- 17 J. He, Y. He, Y. Chen, X. Zhang, C. Hu, J. Zhuang, B. Lei and Y. Liu, Construction and multifunctional applications of carbon dots/PVA nanofibers with phosphorescence and thermally activated delayed fluorescence, *Chem. Eng. J.*, 2018, **347**, 505–513.
- 18 H. Zhao, D. Benetti, X. Tong, H. Zhang, Y. Zhou, G. Liu, D. Ma, S. Sun, Z. M. Wang and Y. Wang, Efficient and stable tandem luminescent solar concentrators based on carbon dots and perovskite quantum dots, *Nano Energy*, 2018, **50**, 756–765.
- 19 L. Gu, H. Shi, C. Miao, Q. Wu, Z. Cheng, S. Cai, M. Gu, C. Ma, W. Yao, Y. Gao, Z. An and W. Huang, Prolonging the lifetime of ultralong organic phosphorescence through dihydrogen bonding, *J. Mater. Chem. C*, 2018, **6**, 226–233.
- 20 D. Zhang, W. Zhou, Q. Liu and Z. Xia,  $\text{CH}_3\text{NH}_3\text{PbBr}_3$  perovskite nanocrystals encapsulated in lanthanide metal-organic frameworks as a photoluminescence converter for anti-counterfeiting, *ACS Appl. Mater. Interfaces*, 2018, **10**, 27875–27884.
- 21 X. Yang and D. Yan, Strongly Enhanced Long-Lived Persistent Room Temperature Phosphorescence Based on the Formation of Metal-Organic Hybrids, *Adv. Opt. Mater.*, 2016, **4**, 897–905.
- 22 H. Q. Yin and X. B. Yin, Multi-Emission from Single Metal-Organic Frameworks under Single Excitation, *Small*, 2021, 2106587.
- 23 Z. Wang, C. Y. Zhu, J. T. Mo, X. Y. Xu, J. Ruan, M. Pan and C. Y. Su, Multi-mode color-tunable long persistent luminescence in single-component coordination polymers, *Angew. Chem., Int. Ed.*, 2021, **133**, 2556–2563.
- 24 S. Cai, H. Ma, H. Shi, H. Wang, X. Wang, L. Xiao, W. Ye, K. Huang, X. Cao and N. Gan, Enabling long-lived organic room temperature phosphorescence in polymers by subunit interlocking, *Nat. Commun.*, 2019, **10**, 1–8.
- 25 W. C. Song, C. C. Geng, S. Y. Li, L. Liang, X. G. Wang, E. C. Yang and X. J. Zhao, Photo-oligomerization by shifting the coordination site in a luminescent coordination polymer, *Commun. Chem.*, 2021, **57**, 2148–2151.
- 26 W. Yin, T. Yu, J. Chen, R. Hu, G. Yang, Y. Zeng and Y. Li, Thermally Activated Upconversion with Metal-Free Sensitizers Enabling Exceptional Anti-Stokes Shift and Anti-counterfeiting Application, *ACS Appl. Mater. Interfaces*, 2021, **13**, 57481–57488.
- 27 W. Tian, J. Zhang, J. Yu, J. Wu, J. Zhang, J. He and F. Wang, Phototunable full-color emission of cellulose-based dynamic fluorescent materials, *Adv. Funct. Mater.*, 2018, **28**, 1703548.

- 28 M. R. Carro-Temboury, R. Arppe, T. Vosch and T. J. Sørensen, An optical authentication system based on imaging of excitation-selected lanthanide luminescence, *Sci. Adv.*, 2018, **4**, e1701384.
- 29 X. Liu, Y. Wang, X. Li, Z. Yi, R. Deng, L. Liang, X. Xie, D. T. Loong, S. Song and D. Fan, Binary temporal upconversion codes of Mn<sup>2+</sup>-activated nanoparticles for multilevel anti-counterfeiting, *Nat. Commun.*, 2017, **8**, 1–7.
- 30 W. You, D. Tu, R. Li, W. Zheng and X. Chen, “Chameleon-like” optical behavior of lanthanide-doped fluoride nanoplates for multilevel anti-counterfeiting applications, *Nano Res.*, 2019, **12**, 1417–1422.
- 31 X. K. Nie, Y. T. Xu, Z. L. Song, D. Ding, F. Gao, H. Liang, L. Chen, X. Bian, Z. Chen and W. Tan, Magnetic-graphitic-nanocapsule templated diacetylene assembly and photopolymerization for sensing and multicolored anti-counterfeiting, *Nanoscale*, 2014, **6**, 13097–13103.
- 32 A. Forni, E. Lucenti, C. Botta and E. Cariati, Metal free room temperature phosphorescence from molecular self-interactions in the solid state, *J. Mater. Chem. C*, 2018, **6**, 4603–4626.
- 33 G. Liu, H. Zhao, F. Diao, Z. Ling and Y. Wang, Stable tandem luminescent solar concentrators based on CdSe/CdS quantum dots and carbon dots, *J. Mater. Chem. C*, 2018, **6**, 10059–10066.
- 34 W. Li, W. Zhou, Z. Zhou, H. Zhang, X. Zhang, J. Zhuang, Y. Liu, B. Lei and C. Hu, A universal strategy for activating the multicolor room-temperature afterglow of carbon dots in a boric acid matrix, *Angew. Chem., Int. Ed.*, 2019, **131**, 7356–7361.
- 35 X. Yu, H. Zhang and J. Yu, Luminescence anti-counterfeiting: From elementary to advanced, *Aggregate*, 2021, **2**, 20–34.
- 36 Y. Sun, S. Liu, L. Sun, S. Wu, G. Hu, X. Pang, A. T. Smith, C. Hu, S. Zeng and W. Wang, Ultralong lifetime and efficient room temperature phosphorescent carbon dots through multi-confinement structure design, *Nat. Commun.*, 2020, **11**, 1–11.
- 37 S. Xu, R. Chen, C. Zheng and W. Huang, Excited state modulation for organic afterglow: materials and applications, *Adv. Mater.*, 2016, **28**, 9920–9940.
- 38 B. Fang, L. Lai, M. Fan and M. Yin, Designing organic room temperature phosphorescence with ultralong lifetime by substituent modification, *J. Mater. Chem. C*, 2021, **9**, 11172–11179.
- 39 Z. Zhou, E. V. Ushakova, E. Liu, X. Bao, D. Li, D. Zhou, Z. Tan, S. Qu and A. L. Rogach, A co-crystallization induced surface modification strategy with cyanuric acid modulates the bandgap emission of carbon dots, *Nanoscale*, 2020, **12**, 10987–10993.
- 40 F. Li, C. Qian, J. Lu, Y. Ma, K. Y. Zhang, S. Liu and Q. Zhao, Color-Tunable Dual Persistent Emission Via a Triplet Exciton Reservoir for Temperature Sensing and Anti-Counterfeiting, *Adv. Opt. Mater.*, 2021, **10**, 2101773.
- 41 Y. Yang, Y. Liang, Y. Zheng, J. A. Li, S. Wu, H. Zhang, T. Huang, S. Luo, C. Liu, G. Shi, F. Sun, Z. Chi and B. Xu, Efficient and Color-Tunable Dual-Mode Afterglow from Large-Area and Flexible Polymer-Based Transparent Films for Anti-Counterfeiting and Information Encryption, *Angew. Chem., Int. Ed.*, 2022, e202201820.
- 42 J. Tan, Q. Li, S. Meng, Y. Li, J. Yang, Y. Ye, Z. Tang, S. Qu and X. Ren, Time-Dependent Phosphorescence Colors from Carbon Dots for Advanced Dynamic Information Encryption, *Adv. Mater.*, 2021, **33**, e2006781.
- 43 X. Wang, H. Ma, M. Gu, C. Lin, N. Gan, Z. Xie, H. Wang, L. Bian, L. Fu and S. Cai, Multicolor ultralong organic phosphorescence through alkyl engineering for 4D coding applications, *Chem. Mater.*, 2019, **31**, 5584–5591.
- 44 Y. Wang, K. Jiang, J. Du, L. Zheng, Y. Li, Z. Li and H. Lin, Green and Near-Infrared Dual-Mode Afterglow of Carbon Dots and Their Applications for Confidential Information Readout, *Nanomicro Lett.*, 2021, **13**, 198.
- 45 T. Sun, B. Xu, B. Chen, X. Chen, M. Li, P. Shi and F. Wang, Anti-counterfeiting patterns encrypted with multi-mode luminescent nanotagants, *Nanoscale*, 2017, **9**, 2701–2705.
- 46 J. Wang, J. Ma, J. Zhang, Y. Fan, W. Wang, J. Sang, Z. Ma and H. Li, Advanced Dynamic Photoluminescent Material for Dynamic Anticounterfeiting and Encryption, *ACS Appl. Mater. Interfaces*, 2019, **11**, 35871–35878.
- 47 X. Yu, K. Liu, H. Zhang, B. Wang, W. Ma, J. Li and J. Yu, Carbon Dots-in-EuAPO-5 Zeolite: Triple-Emission for Multi-level Luminescence Anti-Counterfeiting, *Small*, 2021, **17**, e2103374.
- 48 J. Du, L. Sheng, Q. Chen, Y. Xu, W. Li, X. Wang, M. Li and S. X. A. Zhang, Simple and general platform for highly adjustable thermochromic fluorescent materials and multi-feasible applications, *Mater. Horiz.*, 2019, **6**, 1654–1662.
- 49 Z. Ma, J. Zhou, J. Zhang, S. Zeng, H. Zhou, A. T. Smith, W. Wang, L. Sun and Z. Wang, Mechanics-induced triple-mode anticounterfeiting and moving tactile sensing by simultaneously utilizing instantaneous and persistent mechanoluminescence, *Mater. Horiz.*, 2019, **6**, 2003–2008.
- 50 H. Yang, Y. Liu, Z. Guo, B. Lei, J. Zhuang, X. Zhang, Z. Liu and C. Hu, Hydrophobic carbon dots with blue dispersed emission and red aggregation-induced emission, *Nat. Commun.*, 2019, **10**, 1789.
- 51 Y. Sun, G. Wang, X. Li, B. Zhou and K. Zhang, Achieving High Afterglow Brightness in Organic Dopant-Matrix Systems, *Adv. Opt. Mater.*, 2021, **9**, 2100353.
- 52 Q. Li, M. Zhou, M. Yang, Q. Yang, Z. Zhang and J. Shi, Induction of long-lived room temperature phosphorescence of carbon dots by water in hydrogen-bonded matrices, *Nat. Commun.*, 2018, **9**, 734.
- 53 S. Han, G. Lian, X. Zhang, Z. Cao, Q. Wang, D. Cui and C.-P. Wong, Achieving long lifetime of pure organic room-temperature phosphorescence via constructing hydrogen-bonded organic frameworks, *J. Lumin.*, 2021, **236**, 118120.
- 54 W. Lü, F. Meng and J. Xu, Simple and Highly Efficient Synthesis of Cyanuric Acid by Hydrothermal Method, *Chin. J. Appl. Chem.*, 2020, **37**, 155.
- 55 H. Cheng, W. Sun, Y. Lu, H. Li, W. Su, J. Zhang, T. Guo, F. Li, P. S. Francis and Y. Zheng, Hot electrons in carbon nitride

- with ultralong lifetime and their application in reversible dynamic color displays, *Cell Rep. Phys. Sci.*, 2021, **2**, 100516.
- 56 L. Lin, Z. Yu and X. Wang, Crystalline carbon nitride semiconductors for photocatalytic water splitting, *Angew. Chem., Int. Ed.*, 2019, **131**, 6225–6236.
- 57 A. Hayer, H. Bässler, B. Falk and S. Schrader, Delayed fluorescence and phosphorescence from polyphenylquinoxalines, *J. Phys. Chem. A*, 2002, **106**, 11045–11053.
- 58 J. He, Y. Chen, Y. He, X. Xu, B. Lei, H. Zhang, J. Zhuang, C. Hu and Y. Liu, Anchoring carbon nanodots onto nanosilica for phosphorescence enhancement and delayed fluorescence nascence in solid and liquid states, *Small*, 2020, **16**, 2005228.
- 59 R. Spencer and G. Weber, Influence of Brownian rotations and energy transfer upon the measurements of fluorescence lifetime, *J. Chem. Phys.*, 1970, **52**, 1654–1663.
- 60 G. Baryshnikov, B. Minaev and H. Agren, Theory and Calculation of the Phosphorescence Phenomenon, *Chem. Rev.*, 2017, **117**, 6500–6537.
- 61 J. C. Del Valle and J. Catalan, Kasha's rule: a reappraisal, *Phys. Chem. Chem. Phys.*, 2019, **21**, 10061–10069.
- 62 H. Uoyama, K. Goushi, K. Shizu, H. Nomura and C. Adachi, Highly efficient organic light-emitting diodes from delayed fluorescence, *Nature*, 2012, **492**, 234–238.
- 63 R. Kabe and C. Adachi, Organic long persistent luminescence, *Nature*, 2017, **550**, 384–387.
- 64 H. Wei, L. Gao, K. Fan, J. Liu, J. He, X. Qu, S. Dong, E. Wang and X. Yan, Nanozymes: A clear definition with fuzzy edges, *Nano Today*, 2021, **40**, 101269.
- 65 R. Zhang, X. Yan and K. Fan, Nanozymes inspired by natural enzymes, *Acc. Chem. Res.*, 2021, **2**, 534–547.
- 66 Z. Li, W. Liu, P. Ni, C. Zhang, B. Wang, G. Duan, C. Chen, Y. Jiang and Y. Lu, Carbon dots confined in N-doped carbon as peroxidase-like nanozyme for detection of gastric cancer relevant D-amino acids, *Chem. Eng. J.*, 2022, **428**, 131396.
- 67 Y. Huang, J. Ren and X. Qu, Nanozymes: classification, catalytic mechanisms, activity regulation, and applications, *Chem. Rev.*, 2019, **119**, 4357–4412.